Received: 1 October 2023 | Revised: 28 February 2024 | Accepted: 21 March 2024

DOI: 10.1002/ctpp.202300114

ORIGINAL ARTICLE

Contributions to Plasma Physics

Development of an implicit electromagnetic capability for a hybrid gyrokinetic ion-fluid electron model

Mikhail Dorf | **Milo Dorr** | **Debojyoti Ghosh**

Lawrence Livermore National Laboratory, Livermore, California, USA

Correspondence
Mikhail Dorf, Lawrence Livermore National Laboratory, Livermore, CA, USA.
Email: dorf1@llnl.gov

Funding information
U.S. Department of Energy, Grant/Award Number: DE-AC52-07NA27344

Abstract

We report on the development and implementation of a hybrid kinetic ion–fluid electron model for electromagnetic COGENT simulations of edge plasmas. COGENT is a finite-volume gyrokinetic code that employs a locally field-aligned coordinate system combined with a mapped multi-block grid technology to handle strongly anisotropic edge plasma turbulence. The simulation model involves the long-wavelength limit of the ion gyrokinetic equation coupled to the vorticity and Ohm's law equations for the electromagnetic field perturbations. In order to handle the fast Alfvén wave time scales, an implicit-explicit time integration approach with a physics-based preconditioner is used. The model is successfully applied to the simulations of ion-scale resistive-drift ballooning turbulence in a toroidal annulus geometry. Substantial speed-up over a fully explicit time integration approach is observed.

KEYWORDS

gyrokinetics, implicit methods, tokamak edge

1 | INTRODUCTION

Electromagnetic effects become increasingly important for gyrokinetic[1–3] or drift-fluid[4–8] modeling of microturbulence in a tokamak edge where the presence of steep gradients, e.g., at the L-H transitions and above, makes the characteristic drift frequency, $\omega_{dr} \sim V_s/L_p$, comparable with the Alfvén transit frequency, $\omega_A \sim V_A/qR$. Here, $V_s = \sqrt{T_e/m_i}$ and $V_A = B/\sqrt{4\pi n_i m_i}$ denote the ion sound speed and the Alfvén wave speed, respectively, L_p is the length scale for variations in background plasma profiles, R is the major radius, and q is the magnetic safety factor. At the same time, the performance of explicit time integration methods can suffer from a severe Courant constraint, $\Delta t < h_\parallel/V_A$, where $h_\parallel$ denotes a cell-size in the direction parallel to a magnetic field. Indeed, if the same electromagnetic simulation model is used to describe edge transition from shallower (e.g., L mode) to steeper (e.g., H-mode) gradients, then an explicit scheme might be inefficient for the shallow-gradient state where $\omega_{dr} < V_A/qR$. Moreover, even for a steeper gradient state, strong variations in plasma density, n, across the edge and pronounced variations in the toroidal magnetic field, $B_\phi \propto 1/R$, between the high and low field side can result in severely limited time steps in the spatial regions with a smaller plasma density and a larger magnetic field. Therefore, it is important to develop an implicit time integration scheme, which removes the Courant time step limitation and allows stepping over the fast Alfvén wave time scale, where it is substantially smaller than the time scale of interest (e.g., drift-wave time period).

Implicit calculations typically require solving a nonlinear or linear system of equations at each time step and are therefore more expensive per time step. However, for the case of a hybrid model, which employs 5D

 © 2024 Wiley-VCH GmbH

gyrokinetic ions and 3D drift-fluid electrons, the fast Alfvén time scales are contained within the low-dimensional fluid/field part of the hybrid system, whereas the high-dimensional ion gyrokinetic response occurs on slower drift and ion transient time scales. Consequently, we can apply implicit methods only to fluid electrons, while treating kinetic ions explicitly. In this situation, the computational expense for performing implicit time integration for the 3D electron system can still be less than that of an explicit time step for the 5D kinetic ion system.

An Implicit-Explicit (IMEX) hybrid gyrokinetic ion-fluid electron model has been implemented in the finite-volume code COGENT developed for edge plasma modeling.[9–11] The code solves full-F gyrokinetic equations for an arbitrary number of plasma species with a range of increasingly detailed collision models including the nonlinear Fokker-Planck operator.[12] The gyrokinetic system can also be coupled to a set of lower dimensionality fluid equations in cases where a reduced fluid model is adopted to describe electrons or neutrals. Note that, for a continuum approach, the same discretization method developed for solving hyperbolic PDEs in X-point geometries can be applied to a PDE of arbitrary dimensionality; therefore, supplementing a kinetic simulation model with fluid equations is straightforward. COGENT's numerical discretization is distinguished by making use of a locally field-aligned coordinate system combined with a mapped multi-block grid technology to effectively handle strongly anisotropic turbulence in an X-point geometry. In this approach, the toroidal direction is divided into blocks, such that within each block, the cells are field-aligned and a nonmatching (non-conformal) grid interface is allowed at block boundaries. The toroidal angle corresponds to the "coarse" field-aligned coordinate, whereas the poloidal cross section, comprising the radial and poloidal directions, is finely gridded to resolve short-scale perpendicular turbulence and to support accurate re-mapping (interpolation) at block boundaries.[9]

The electrostatic version of the IMEX hybrid model has been previously verified and applied to simulations of the ion-scale turbulence in a tokamak edge.[9,13] Here, we extend the hybrid model to include electromagnetic effects. The IMEX time integration algorithm used in COGENT is based on semi-implicit additive Runge–Kutta (ARK) methods[14] and can provide consistent high-order time integration, including implicit treatment of selected stiff terms.[15] It employs the Jacobian-free Newton-Krylov (JFNK) approach[16] to handle nonlinearities and utilizes preconditioning to improve convergence properties. In the present work, a physics-based preconditioner, which captures linear Alfvén dynamics along with the resistive and electron inertia effects, is used to facilitate the implicit time integration. The preconditioner operator yields a sparse linear system that is solved by making use of algebraic multigrid methods contained in the hypre linear solver library.[17]

The paper is organized as follows. The simulation model and the IMEX approach are described in Section 2. The electromagnetic/fluid part of the model is verified within a context of a simple three-field fluid model in Section 3. Verification simulations include comparison with an analytical theory for the case of a uniform slab geometry in Section 3.1, and for the case of a tilted slab geometry in Section 3.2. The latter verifies the field-aligned discretization and re-mapping at the toroidal block boundaries. In Section 3.3, the performance of the implicit time integration is analyzed for the case of the resistive ballooning instability (RBI) in a toroidal annulus geometry. Finally, Section 4 presents the preliminary results of proof-of-principle electromagnetic COGENT simulations for the case of the resistive-drift ballooning turbulence performed with the hybrid gyrokinetic ion-fluid electron model.

2 | NUMERICAL MODEL

The electromagnetic version of the hybrid gyrokinetic ion-fluid electron simulation model employed in the COGENT code includes the full-F gyrokinetic equation for the ion species distribution function, $f_i(\mathbf{R}, v_\parallel, \mu)$, coupled to the quasineutrality equation for the vorticity variable, ϖ, and to the Ohm's law equation for the parallel vector potential, $A_\parallel$. Note that the edge of a tokamak is distinguished by a low value of the β parameter (plasma pressure is small compared with magnetic field pressure) and by the strongly anisotropic nature of drift microturbulence with $k_\perp \gg k_\parallel$. As a result, one can neglect the perpendicular component of the vector potential, $\mathbf{A}$, that describes the compressional Alfvén wave, and only retain the shear Alfvén wave, $\omega_A = k_\parallel V_A$. Furthermore, for simplicity purposes, here we neglect electromagnetic flutter effects that correspond to B-field perturbations and only retain the electromagnetic induction in the parallel electric field, $E_\parallel = -\nabla_\parallel \Phi - c^{-1}\partial A_\parallel/\partial t$. Although the former effects generate peeling instabilities that are important, for instance, for the analysis of MHD stability and ELM properties,[6] they may be of lesser importance in the context of L-mode transport.[8]

2.1 | Hybrid model description

Adopting the long-wavelength limit, $k_\perp \rho_i \ll 1$, the ion gyrokinetic equation takes the following form:

$$\frac{\partial\left(B_\parallel^* f_i\right)}{\partial t} + \nabla \cdot \left(\dot{\mathbf{R}} B_\parallel^* f_i\right) + \frac{\partial}{\partial v_\parallel}\left(\dot{v}_\parallel \boldsymbol{B}_\parallel^* f_i\right) = C\left(\boldsymbol{B}_\parallel^* f_i\right), \tag{1}$$

$$\dot{\mathbf{R}} = \frac{1}{B_\parallel^*}\left[v_\parallel \mathbf{B}^* + \frac{c}{Z_i e}\mathbf{b} \times (Z_i e \nabla \Phi + \mu \nabla B)\right], \tag{2}$$

$$\dot{v}_\parallel = -\frac{1}{m_i B_\parallel^*}\mathbf{B}^* \cdot (Z_i e \nabla \Phi + \mu \nabla B) - \frac{Z_i e}{m_i c}\frac{\partial A_\parallel}{\partial t}, \tag{3}$$

Here, m_i and Z_i are the ion species mass and charge state, respectively, $-e$ is the electron charge, c is the speed of light, $\mathbf{B} = B\mathbf{b}$ is the magnetic field with $\mathbf{b}$ denoting the unit vector along the field, $\mathbf{B}^*\left(\mathbf{R}, v_\parallel\right) \equiv \mathbf{B} + (m_i c/Z_i e) v_\parallel \nabla \times \mathbf{b}$, $B_\parallel^* = \mathbf{B}^* \cdot \mathbf{b}$ is the Jacobian of the transformation to the gyrocenter coordinates $\left(\mathbf{R}, v_\parallel, \mu\right)$, $\rho_i = V_{Ti}/\Omega_i$ is the ion thermal gyroradius, $V_{Ti} = \sqrt{T_i/m_i}$ is the ion thermal velocity, $\Omega_i = Z_i e B/(m_i c)$ is the cyclotron frequency, and $k_\perp^{-1}$ represents the characteristic length scale for variations in the electromagnetic fields. Although a wide range of detailed collision models $C\left(B_\parallel^* f_i\right)$ including the full nonlinear Fokker-Planck operator is available in COGENT,[12] for simplicity purposes, we do not include ion collisions in this work.

Self-consistent variations of an electrostatic potential are described by making use of the quasi-neutrality equation ($\nabla \cdot \mathbf{j} = 0$) for the vorticity variable[9]:

$$\varpi = \nabla_\perp \cdot \left(\frac{c^2 n_i m_i}{B^2}\nabla_\perp \Phi\right), \tag{4}$$

$$\frac{\partial \varpi}{\partial t} + \nabla \cdot \left(c\frac{-\nabla_\perp \Phi \times \mathbf{b}}{B}\varpi\right) = \nabla \cdot \left(\frac{2\pi Z_i e}{m_i}\int \mathbf{v}_\perp^m f_i B_\parallel^* dv_\parallel d\mu\right) + \nabla \cdot \left[\frac{c Z_i n_i T_e}{B}\left(\nabla \times \mathbf{b} + \frac{\mathbf{b} \times \nabla B}{B}\right)\right] + B\nabla_\parallel\left(\frac{j_\parallel}{B}\right). \tag{5}$$

Here, $\nabla_\perp = \nabla - \mathbf{b}(\mathbf{b} \cdot \nabla)$, $\mathbf{v}_\perp^m \equiv \mathbf{R}_\perp(\Phi = 0)$ is the magnetic drift velocity corresponding to the perpendicular component of the guiding center velocity in Equation (2) for the case of a zero potential, T_e is the electron temperature, and the ion gyrocenter density, n_i, is given by

$$n_i = \frac{2\pi}{m_i}\int f_i B_\parallel^* dv_\parallel d\mu. \tag{6}$$

We note that the simplified quasi-neutrality model in Equations (4)–(5) does not include $O\left(k^2\rho_i^2\right)$ finite-Larmor-radius or $O\left(k^2\rho_s^2\right)$ polarization density corrections, thereby employing the ion gyrocenter density, n_i, and not the electron density, n_e, in the second term on the RHS of Equation (6) that describes the divergence of the perpendicular electron current. Also, the parallel advection of the vorticity variable is neglected.

The parallel current in Equation (5) is determined by making use of the parallel Ampere's law:

$$j_\parallel = -\frac{c}{4\pi}\Delta_\perp A_\parallel, \tag{7}$$

where the perpendicular Laplacian operator is defined as $\Delta_\perp \equiv \nabla_\perp^2$. Finally, variations in the parallel vector potential are described by Ohm's law, which can be derived from the equation for electron parallel momentum:

$$m_e\left[\frac{\partial v_{\parallel e}}{\partial t} + (\mathbf{V}_e \cdot \nabla)v_{\parallel e}\right] = e\nabla_\parallel \Phi + \frac{e}{c}\frac{\partial A_\parallel}{\partial t} - \frac{\nabla_\parallel (n_e T_e)}{n_e} + e\frac{j_\parallel}{\sigma_\parallel} - 0.71\nabla_\parallel T_e.$$

Here, the last two terms on the right hand side correspond to the electron friction force[18] $R_{\parallel ei} = e j_\parallel/\sigma_\parallel - 0.71\nabla_\parallel T_e$, where $\sigma_\parallel = 1.96 n_e e^2 \tau_e/m_e$ is the parallel electron conductivity, and τ_e denotes the electron collisional time. For simplicity purposes, here we assume $v_{e\parallel} \approx -j_\parallel/(e n_e)$ and neglect the convective advection term, $(\mathbf{V}_e \cdot \nabla)v_{\parallel e}$, to obtain the following

model equation for the parallel vector potential, $A_\parallel$:

$$\frac{1}{c}\frac{\partial}{\partial t}\left[\left(1-\frac{m_e c^2}{4\pi e^2 Z_i n_i}\Delta_\perp\right)A_\parallel\right] = -\nabla_\parallel \Phi + \frac{\nabla_\parallel (n_e T_e)}{eZ_i n_i} + \frac{c}{4\pi\sigma_\parallel}\Delta_\perp A_\parallel + \frac{0.71}{e}\nabla_\parallel T_e. \tag{8}$$

We again neglect a small difference between the electron density and ion gyrocenter density in Equation (8) except for the ~~parallel~~ electron pressure term, where retaining the polarization density correction:

$$n_e = \nabla_\perp \cdot \left(\frac{c^2 m_i n_i}{eB^2}\nabla_\perp \Phi\right) + Z_i n_i, \tag{9}$$

is found to be important to provide stabilization of high-$k\rho_{i,s}$ perturbations. Assuming slow time variations of the background plasma density, we compute the term $c^{-1}\partial A_\parallel/\partial t$ that appears in Equation (3) by applying the operator $\left(1-\frac{m_e c^2}{4\pi e^2 Z_i n_i}\Delta_\perp\right)^{-1}$ to the RHS of Equation (8). Finally, equations (1)–(9) for the ion distribution function and electromagnetic potentials need to be coupled to a model for an electron temperature. For the present purposes, a simplified isothermal response $T_e = const$ is assumed.

2.2 | IMEX time integration approach

To circumvent limitations of explicit time integration related to the tight Courant time step constraint, $\Delta t < h_\parallel/V_A$, an implicit-explicit (IMEX) approach is utilized in COGENT.[9,15] Detailed description of the IMEX algorithm for the hybrid COGENT model will be reported elsewhere, and here, we only briefly summarize the key elements of the approach. The implicit part of the problem corresponds to the following subset of the full system:

$$\frac{\partial \varpi}{\partial t} = \nabla \cdot \left(-\frac{c}{4\pi}\mathbf{b}\Delta_\perp A_\parallel\right), \tag{10}$$

$$\frac{1}{c}\frac{\partial}{\partial t}\left[\left(1-\frac{m_e c^2}{4\pi e^2 Z_i n_i}\Delta_\perp\right)A_\parallel\right] = -\nabla_\parallel \Phi + \frac{c}{4\pi\sigma_\parallel}\Delta_\perp A_\parallel + \frac{\nabla_\parallel (\varpi T_e)}{e^2 Z_i n_i}, \tag{11}$$

which includes the linear effects of shear Alfvén waves, plasma resistivity, and electron inertia. The last term on the RHS of Equation (11) corresponds to the polarization density corrections in the electron parallel pressure term. The rest of the hybrid system includes the ion transient, $\omega_{tr,i} \sim k_\parallel V_{Ti}$, and drift wave, $\omega_{dr} \sim (k_\perp \rho_s)V_s/L_p$, frequencies and is treated explicitly. After performing time discretization, the IMEX approach requires solving the following linear system at the implicit stages of an ARK time step:

$$\alpha\nabla_\perp \cdot \left(\frac{c^2 n_i m_i}{B^2}\nabla_\perp \Phi\right) + \frac{c}{4\pi}\nabla \cdot \left(\mathbf{b}\Delta_\perp A_\parallel\right) = r_\Phi, \tag{12}$$

$$\frac{1}{c}\left[\alpha - \left(\alpha + 0.51\tau_e^{-1}\right)\frac{c^2}{\omega_{pe}^2}\Delta_\perp\right]A_\parallel + \nabla_\parallel \Phi - \frac{T_e}{e^2 Z_i n_i}\nabla_\parallel\left(\nabla_\perp \cdot \left(\frac{c^2 n_i m_i}{B^2}\nabla_\perp \Phi\right)\right) = r_A. \tag{13}$$

Here, $\omega_{pe}^2 = 4\pi e^2 Z_i n_i/m_e$ is the electron plasma frequency, $\alpha \propto \Delta t^{-1}$ is a constant coefficient dependent on the order of the ARK scheme and the stage number, and $r_\Phi(\mathbf{R})$ and $r_A(\mathbf{R})$ are the spatial functions that include contributions from the previous implicit and explicit stages. The linear system in Equations (12)–(13) is solved by making use of the GMRES algorithm that approximates the solution by a vector in a Krylov subspace with minimal residual.[19] The GMRES method does not require the assembly and storage of a sparse matrix corresponding to a spatially discretized version of the linear system. Instead, it only involves evaluating a linear operator action on a vector, making it straightforward to implement.[16] However, the convergence properties of the iterative GMRES solver strongly depend on preconditioning. Here, a physical preconditioner that approximates the implicit linear system in Equations (12)–(13) is developed as follows.

First, the solution to Equation (12) is approximated as

$$\Phi \simeq \frac{B^2}{\alpha c^2 m_i n_i}\left(-\frac{c}{4\pi}\nabla \cdot \left(\mathbf{b}A_\parallel\right) + \Delta_\perp^{-1} r_\Phi\right). \tag{14}$$

In deriving Equation (14) we made use of $\nabla_\perp \cdot \left(c^2 n_i m_i B^{-2} \nabla_\perp \Phi\right) \simeq \Delta_\perp \left(c^2 n_i m_i B^{-2} \Phi\right)$ and $\nabla \cdot \left(\boldsymbol{b} \Delta_\perp A_\parallel\right) \simeq \Delta_\perp \left(\nabla \cdot \left(\boldsymbol{b} A_\parallel\right)\right)$. The former is valid in the limit where the perpendicular wavenumber of turbulence perturbations in Φ is large compared with the background gradient of plasma density n_i, i.e., $k_\perp \gg L_p^{-1}$. The latter becomes approximately valid in the regime where the parallel wavelength of perturbations in $A_\parallel$ is small compared with the length scale of background magnetic field variations, which is the case for grid-size perturbations, $k_\parallel \sim h_\parallel^{-1}$ determining the fastest time scales. Finally, the same type of boundary conditions, e.g., Dirichlet or Neumann, is assumed for the Φ and $A_\parallel$ variables at the perpendicular domain boundaries.

The approximation for the potential in Equation (14) is then plugged into Equation (13) to obtain the following approximate equation for $A_\parallel$:

$$\frac{1}{c}\left[\alpha - \left(\alpha + 0.51\tau_e^{-1}\right)\frac{c^2}{\omega_{pe}^2}\Delta_\perp\right] A_\parallel - \frac{1}{\alpha c}\nabla_\parallel\left(V_A^2 B \nabla_\parallel\left(\frac{A_\parallel}{B}\right)\right) \simeq r_A - \nabla_\parallel\left(\frac{B^2}{\alpha c^2 m_i n_i}\Delta_\perp^{-1} r_\Phi\right). \tag{15}$$

Here, $V_A = \sqrt{B^2/4\pi n_i m_i}$ is the Alfvén velocity, and we neglect the high-order polarization density correction term, i.e., the last term on the LHS of Equation (13). Equations (14)–(15) are used to precondition the solution of the implicit linear system in Equations (12)–(13). We emphasize that the approximations made in deriving the preconditioner system do not affect the accuracy of the GMRES solution, because preconditioning is only used to improve the efficiency of a GMRES solver. The preconditioner system involves two 3D positive-definite, second-order elliptic operators: the negative perpendicular Laplacian operator, $-\Delta_\perp$, and the operator corresponding to the LHS of Equation (15), which are efficiently solved by making use of algebraic multigrid (AMG) solvers contained in the hypre linear solver library.[17] In order to use the AMG methods, the corresponding sparse matrices need to be assembled and stored. In addition to other interfaces, hypre provides a semi-structured interface, which is well suited for systems resulting from the multi-block discretizations employed in COGENT. Due to the irregular stencil couplings at interblock boundaries, hypre's BoomerAMG algebraic multigrid solver is used.

In conclusion, it is instructive to note that a conceptually similar physical preconditioner was developed for the BOUT++ code[20]; however, the resistive and the electron inertia terms producing radial couplings were not included. That simplification, together with the choice of the coarse coordinate corresponding to the poloidal (instead of the toroidal) angle enables convenient representation of the preconditioner system by a large number of independent 1D equations for the parallel elliptic operator. The 3D multigrid solver capability utilized here can, however, facilitate a broader range of elliptic problems that include both parallel and perpendicular coupling. This is the case for COGENT preconditioner operators developed for the electromagnetic [see Equation (15)] and electrostatic[9] versions of the hybrid model.

3 | VERIFICATION STUDIES

In this section, we present the results of linear verification studies that test the 3D fluid/field part of the hybrid model. For these purposes, we replace the gyrokinetic ion response in Equations (1)–(3) with a minimal cold drift-fluid model, which only includes the $E \times B$ advection term

$$\frac{\partial \delta n_i}{\partial t} + \nabla \cdot \left(c\frac{-\nabla\, \Phi \times \mathbf{b}}{B} n_0\right) = 0, \tag{16}$$

where n_0 and δn_i denote the background and perturbation ion density, respectively. Accordingly, the divergence of the ion perpendicular current, i.e., the first term on the RHS of Equation (5), and the nonlinear Reynolds-Stress term, i.e., the second term on the LHS of Equation (5), are not included in the verification model.

3.1 | Uniform slab test case

Consider a uniform slab geometry $\mathbf{R} = (x, y, z)$ with $\mathbf{B} = (0, B, 0)$ for which the linearized version of Equations (5)–(8) takes the following form:

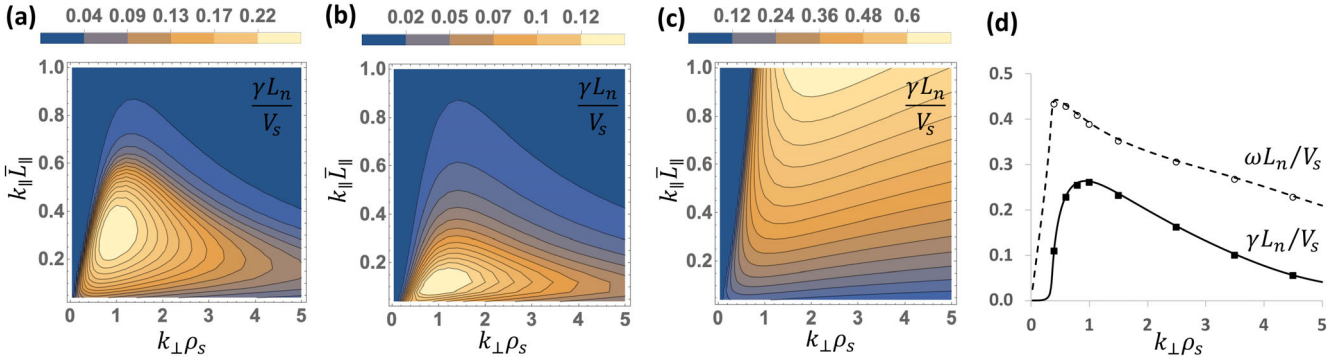

FIGURE 1 Linear regime of the electromagnetic drift-resistive instability for a uniform slab geometry. Shown are numerical solutions to the linear dispersion relation for (a) electromagnetic case, (b) electrostatic case, and (c) electromagnetic case without the polarization density correction term. Frame (d) illustrates the comparison between the linear COGENT simulations (squares and dots) and the numerical solution to the electromagnetic dispersion relation (solid and dashed curves) for $k_\parallel \bar{L}_\parallel = 0.3$. Here, $\rho_s = V_s/\omega_{ci} = 0.7$ mm is the ion sound gyroradius and $\bar{L}_\parallel = 1.0$ m is the normalization factor for the parallel length scales.

$$\frac{\partial}{\partial t}\delta\varpi = -\frac{c}{4\pi}\nabla_\parallel\left(\Delta_\perp \delta A_\parallel\right), \tag{17}$$

$$\left(1 - \frac{m_e c^2}{4\pi e^2 Z_i n_0}\Delta_\perp\right)\frac{1}{c}\frac{\partial}{\partial t}\delta A_\parallel = -\nabla_\parallel \delta\Phi + \frac{T_e}{eZ_i n_0}\nabla_\parallel\left(Z_i\delta n_i + e^{-1}\varpi\right) + \frac{c}{4\pi\sigma_\parallel}\Delta_\perp\delta A_\parallel. \tag{18}$$

$$\delta\varpi = \nabla_\perp \cdot \left(\frac{c^2 n_0 m_i}{B^2}\nabla_\perp \delta\Phi\right), \tag{19}$$

where $\delta\Phi$ and $\delta A_\parallel$ denote linear perturbations relative to an equilibrium solution with $\Phi_0 = 0$ and $A_{\parallel,0} = 0$. Assuming $L_n k_x \gg 1$ and $k_x \ll k_z$, a numerical solution to the local dispersion relation corresponding to the unstable mode of the linear system in Equations (16)–(19) is shown in Figure 1a for the parameters characteristic of the DIII-D tokamak edge region: $n_0 = 2 \cdot 10^{19}$ m^{-3}, $T_e = 100$ eV, $B = 2$ T, $L_n = n_0|dn_0/dx|^{-1} = 3$cm, $Z_i = 1$, $m_i = 2m_p$. For this choice of parameters, the electrons are moderately collisional with $\tau_e V_{Te}/qR_0 \approx 1$, where we adopt $q = 3.5$, $R_0 = 1.6$ m, and $V_{Te} = \sqrt{T_e/m_e}$. To elucidate the electromagnetic effects, we also plot a numerical solution to the local dispersion relation in the electrostatic limit, which is obtained by neglecting the terms in the LHS of Equation (18). Comparing the results in Figure 1a,b one can observe substantially larger values of the linear growth rate for the electromagnetic case. Finally, Figure 1c illustrates the electromagnetic linear dispersion for the case where the polarization density correction term, $e^{-1}\varpi$, is removed from Equation (18). An unbounded increase in the linear growth rate in the short wavelength part of the spectra [see Figure 1c] can cause numerical issues in COGENT simulations when the stabilizing polarization density correction is not included.

A numerical solution to the dispersion relation for the unstable mode growth rate and frequency is compared with the results of implicit COGENT simulations for the linear physical problem in Equations (16)–(19) [see Figure 1d]. Excellent agreement between the simulations and the theory is observed. The COGENT simulations consider conducting (grounded) boundaries in the x-direction and periodic boundary conditions in the y and z directions. The spatial domain extent for each COGENT simulation in Figure 1d is given by $L_x = 0.1$ m, $L_y = 2\pi/k_y$, $L_z = 2\pi/k_z$, and all harmonics other than the fundamental one are filtered out from the electrostatic, $\delta\Phi$, and vector potential, $\delta A_\parallel$, distributions in the periodic directions y and z after each solve of Equations (17)–(18). The grid resolution is given by $\left(N_x, N_y, N_z\right) = (16,32,32)$.

3.2 | Tilted-B slab test case

To test the field-aligned implementation of the electromagnetic model, we consider a plasma box with dimensions $\left(L_x, L_y, L_z\right)$, which is periodic in the y and z directions, and a uniform magnetic field, which has a tilt relative to the y axis $B = \left(0, B_y, B_z\right)$ [see Figure 2]. This geometry approximates the case of a periodic toroidal annulus wedge with a large aspect ratio and the annulus width much smaller than the minor radius, $(r, R\phi, r\theta) \leftrightarrow (x, y, z)$. Here, θ and ϕ are the poloidal and toroidal angles, respectively. The linear system in Equations (16)–(19) is solved, and a solution for an unstable mode

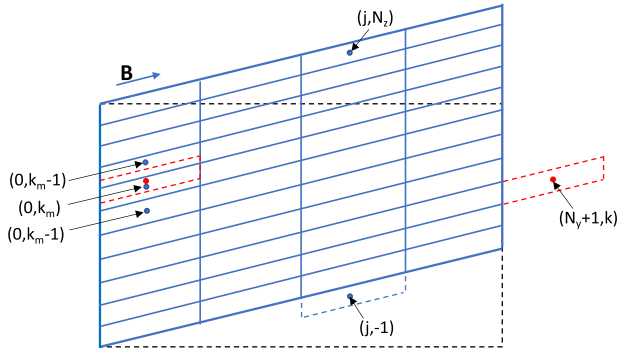

N_z	$\gamma L_n/V_s$	$\delta(\gamma L_n/V_s)$
1024	0.2344	2.3e-2
2048	0.2527	4.6e-3
4096	0.2563	9.7e-4
8192	0.2573	

FIGURE 2 COGENT simulations of the electromagnetic drift-resistive instability for a tilted-B slab geometry. Left panel illustrates the schematic of a locally field-aligned discretization approach. Simulations are performed within the tilted slab computational domain shown in blue, where the periodical boundary conditions are applied both in vertical (poloidal) and horizontal (toroidal) directions. Note that the results of these simulations are equivalent to those performed within the computational domain shown with the dashed lines. The periodicity in the vertical direction yields equal values in the ghost cell $(j,-1)$ and the valid cell (j,N_z). Obtaining the value in the ghost cell (N_y+1,k) requires interpolation from the three valid cells $(0,k_m-1)$, $(0,k_m)$, and $(0,k_m+1)$, where the k_m index is determined from the horizontal periodicity condition. The table in the right panel shows the results of the COGENT convergence studies. The last column corresponds to the difference between the normalized growth rate value for $N_z=8192$ and the corresponding lower resolution values. Slightly better than second-order convergence is observed. Grid resolution in the x and y is maintained fixed at $N_x=16$ and $N_y=4$.

can be readily obtained from the results described in Section 3.1 [see Figure 1] by making use of the following geometric relations:

$$k_{\parallel}=\frac{2\pi n}{L_y}\frac{B_y}{B}+\frac{2\pi m}{L_z}\frac{B_z}{B}, \tag{20}$$

$$k_{\perp}=\frac{2\pi n}{L_y}\frac{B_z}{B}-\frac{2\pi m}{L_z}\frac{B_y}{B}, \tag{21}$$

where, $B=\sqrt{B_y^2+B_z^2}$ and (n,m) are integer numbers defining the mode wavelength in the (y,z) directions that is supported by the domain periodicity. Tokamak drift microturbulence is characterized by strong anisotropy, where $k_{\parallel}$ is much smaller than $k_{\perp}$. Therefore, to facilitate numerical simulations, a locally field-aligned coordinate system is used in COGENT.[9]

For the case of a tilted slab geometry this approach is illustrated in Figure 2a. Because the toroidal cell faces at the toroidal boundaries do not conform, imposing the periodicity condition necessitates interpolation in the finely gridded poloidal direction. It is instructive to note that for the case of a slab geometry, the COGENT approach is similar to the flux coordinate independent (FCI) discretization proposed in Reference [21] and used, for instance, in Reference.[8] However, for the case of an X-point geometry, the COGENT approach retains the magnetic flux surfaces as a radial coordinate to minimize possible numerical pollution error.[9] This is in contrast to the FCI approach, where the standard cylindrical or Cartesian coordinate systems are employed in the poloidal plane. For all simulations discussed below, we use a single toroidal block with re-mapping/interpolation included only at domain boundaries. This is justified for the case where the size of the toroidal domain is small and the grid distortions due magnetic shear are tolerable. In order to mitigate the effects of magnetic shear, COGENT adopts a multi-block discretization in the toroidal direction. Field-aligned mappings are defined in the same way in each toroidal block and re-mapping occurs at toroidal block interfaces. More details regarding the COGENT discretization scheme can be found in Reference.[9]

The results of COGENT simulations are shown in Figure 2b. The same plasma parameters as those described in Section 3.1 are used, the magnetic field correspond to $B_y=2$ T, $B_z=0.2$ T, and the domain dimensions are given by $L_x=0.1$m, $L_z=0.52$ m and $L_y=2.63$ m. Initial perturbation is given by a mode with $(m,n)=(113,-57)$, which corresponds to $k_{\perp}\rho_s=1.0$ and $k_{\parallel}\bar{L}_{\parallel}=0.36$ and a nearly maximum growth rate of $\gamma_{(113,-57)}=0.259V_s/L_n$. Here, $\rho_s=V_s/\omega_{ci}=0.7$ mm is the ion sound gyroradius and $\bar{L}_{\parallel}=1.0$ m is the normalization factor. In the x-direction half of the sine wave is used to satisfy zero Dirichlet boundary conditions. No harmonic filtering is performed, and it is instructive to note that these simulations can also support nearby modes with close values of the growth rate, for instance, $\gamma_{(115,-58)}=0.254V_s/L_n$ and

$\gamma_{(111,-56)} = 0.263 V_s/L_n$. Accordingly, it was observed (in separately carried out test studies) that an arbitrary initial perturbation can result in a multimode structure with beating patterns where multiple eigenmodes with close growth rates are simultaneously amplified. In the present simulations, the initial perturbation with a single harmonic pattern in the y and z directions is observed to maintain its structure and to exhibit a growth consistent with the analytical predictions [see Figure 2].

The parallel wavelength for the simulated unstable mode $\lambda_\parallel = 17.45$ m is much larger than the parallel extent of the simulation domain $L_\parallel = \sqrt{L_y^2 + L_z^2} = 2.68$ m. Therefore, only a small fraction, $L_\parallel/\lambda_\parallel \sim 0.15$, of a parallel harmonic is contained within the simulation box, and it can therefore be well resolved with a minimal number of cells in the field-aligned direction. Here, four parallel cells are used, which effectively corresponds to $4/0.15 \approx 27$ cells for a full harmonic. This test case is conceptually similar to the case of tokamak microturbulence modeling, where a small toroidal wedge simulation with $\Delta\phi \ll 2\pi$ can provide good description of microturbulence characterized by large toroidal harmonic numbers with $n\Delta\phi \ll 2\pi$.[7] Accordingly, only a small fraction of a typical parallel wavelength, $\sim 1/qR$, will be contained within the wedge.

At the same time, it is important to note that optimal grid resolution in the fine (perpendicular) and coarse (parallel) directions are related to each other for discretization schemes that involve interpolations for computing parallel derivatives. For the case illustrated in Figure 2a, the truncation error in parallel derivatives at the toroidal boundaries is given by

$$Err\left(\frac{\nabla_\parallel \Phi}{\Phi}\right) \sim \max\left\{ O\left(\frac{\left(h_\parallel/\lambda_\parallel\right)^{p_1}}{\lambda_\parallel}\right), O\left(\frac{(h_z/L_z)^{p_2}}{h_\parallel}\right)\right\}. \tag{22}$$

Here, h_z and $h_\parallel$ is the cell-size in the z (poloidal) and parallel directions, respectively, p_1 is the order of the discretization scheme in the domain interior, and p_2 is the order of the interpolation in the z-direction. For the present studies, $p_1 = 2$ and $p_2 = 3$ are used. Due to the presence of interpolation, the total truncation error [in Equation (22)] can increase unboundedly if the parallel cell-size, $h_\parallel$, decreases while the poloidal cell-size, h_z, is maintained fixed. The convergence properties in the z-direction are illustrated in Figure 2c. Second-order convergence is observed, and it is interesting to note that even $1024/113 \approx 9$ cells per poloidal harmonic are sufficient to recover the growth rate within 10%.

3.3 | IMEX verification

The efficiency of the IMEX approach [see Section 2.2] is demonstrated by considering a resistive ballooning instability (RBI) test case in a toroidal annulus geometry. For these studies, we omit drift-wave effects [the second term on the RHS of Equation (18)], and only retain the ballooning drive, such that Equations (17)–(18) take the following form:

$$\frac{\partial}{\partial t}\delta\varpi = \nabla\cdot\left[\frac{cZ_i\delta n_i T_e}{B}\left(\nabla\times\mathbf{b} + \frac{\mathbf{b}\times\nabla B}{B}\right)\right] - \frac{c}{4\pi}\nabla\cdot\left(\mathbf{b}\Delta_\perp\delta A_\parallel\right), \tag{23}$$

$$\left(1 - \frac{m_e c^2}{4\pi e^2 Z_i n_0}\Delta_\perp\right)\frac{1}{c}\frac{\partial}{\partial t}\delta A_\parallel = -\nabla_\parallel\delta\Phi + \frac{c}{4\pi\sigma_\parallel}\Delta_\perp\delta A_\parallel. \tag{24}$$

A COGENT ~~n~~ solution to the linear system in Equations (16), (19), (23)–(24) is shown in Figure 3 for the following illustrative parameters: $T_e = 400$ eV, $m_i = m_p$, $Z_i = 1$, $I = RB_\phi = -3.5$ Tm, $R_0 = 1.6$ m, $n_0 \sim 10^{20}\text{m}^{-3}$, $q \sim 4$, $L_n \sim 3$ cm. An artificially increased uniform value of the electron collisionality corresponding to $\tau_e V_{T_e}/\left(qR_0\right) = 0.075$ is adopted for the plasma conductivity. Detailed profiles of the initial plasma density, n_0, and magnetic safety factor, q, are shown in Figure 3a. The magnetic geometry, field-aligned coordinate system, and the COGENT spatial discretization are described in detail in References.[9,13] A toroidally periodic wedge, $\Delta\phi = \pi/10$, is considered and the grid resolution is given by $\left(N_r, N_\phi, N_\theta\right) = (64, 8, 1024)$. The characteristic time scales for the Alfvén waves and the ideal ballooning instability correspond to $\omega_A^{-1} \sim qR_0/V_A \sim 1.3$ μs and $\gamma_{bal}^{-1} \sim \sqrt{L_n R_0}/\sqrt{2}V_s \sim 0.9$ μs, respectively.

Figure 3c shows the simulation results obtained by making use of a second-order IMEX time integration[22] with $\Delta t_{imp} = 0.5$ μs and the fourth-order explicit Runge–Kutta scheme with $\Delta t_{exp} = 10$ ns. The explicit time step is close to the CFL-limited value for stable time integration. Increasing Δt_{exp} by 25% causes the simulation to become unstable. Excellent agreement between the explicit and implicit results is observed during the development of the dominant mode,

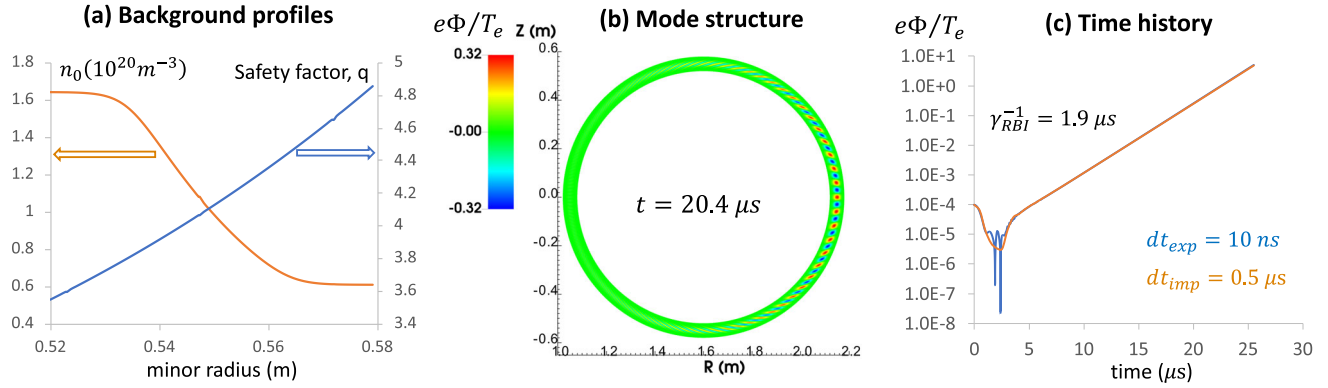

FIGURE 3 COGENT simulations of the resistive ballooning instability showing (a) background profiles for the density and magnetic safety factor, (b) mode structure at $t = 20.4$ μs, and (c) time history of the potential perturbations at the outer midplane for the explicit (blue) and implicit (orange) time integration schemes.

with the inverse growth rate $\gamma_{RBI}^{-1} = 1.9$ μs. During the initial transient stage, the presence of the fast Alfvén waves with a small energy content leads to the degraded accuracy of the implicit methods that do not resolve the Alfvén time scale. As described in Section 2.2, the IMEX approach involves solving the linear system in Equations (12)–(13) by making use of the GMRES algorithm. It is observed that an unpreconditioned GMRES solver fails to converge, while the use of the preconditioner in Equations (14)–(15) reduces the GMRES solver residual by the six orders of magnitude in approximately 10 iterations. The COGENT simulations are performed on 128 CPU cores of the NERSC Perlmutter cluster and it takes about 5.5 and 1.2 s of wall clock time per step for the IMEX and explicit time integration schemes, respectively. As a result, the IMEX approach speeds up simulations of a given time period by a factor of 11.

4 | HYBRID SIMULATION RESULTS

Illustrative nonlinear simulations of the resistive-drift ballooning turbulence are performed with the locally field-aligned IMEX electromagnetic hybrid model [in Equations (1)–(9)] for the case of the toroidal annulus geometry specified in Section 3.3. For simplicity purposes and to further enhance the turbulence, possible mitigating factors such as ion-ion collisions and Reynolds-stress term are not included in the present studies. A collocated cell-centered discretization, which is used for both the electrostatic potential Φ and parallel vector potential $A_\parallel$, is prone to the so-called odd-even numerical Nyquist instability, which is controlled in the present studies by adding a small numerical parallel hyperviscosity term. To further stabilize the simulations, we add small perpendicular hyperviscosity in the entire domain and additionally suppress turbulence perturbations at the inner core boundary.

The phase-space advection operator in the ion gyrokinetic equation [Equation (1)] requires specification of inflow fluxes at the phase-space boundaries. In the present work, inflow fluxes are generated by a Maxwellian distribution located at a domain boundary and characterized by the initial values for ion density, $n_0(r)$, temperature $T_0(r)$, and parallel velocity, $V_0(r)$. Boundary conditions for the electrostatic potential Φ include a zero Dirichlet boundary condition on the outer radial boundary and the following "consistency" condition at the inner radial boundary:

$$\left\langle \frac{c^2 n_i m_i}{B^2} |\nabla\psi|^2 \right\rangle \frac{\partial \Phi}{\partial \psi} = \int_0^t dt \left\langle \nabla\psi \cdot \mathbf{j}_i \right\rangle. \tag{25}$$

Here, $\mathbf{j}_i = (2\pi Z_i e/m_i) \int \dot{\mathbf{R}} f_i B_\parallel^* dv_\parallel d\mu$ is the ion gyrocenter current density and $\langle \chi \rangle$ is the flux-surface average defined as the volume average of χ between two neighboring flux surfaces, ψ and $\psi + d\psi$. The boundary condition for the vector potential variable $A_\parallel$ corresponds to a zero Dirichlet BC at the outer radial boundary and a zero Neumann BC at the inner radial boundary.

The initial distribution for a deuterium ion plasma ($Z_i = 1$, $m_i = 2m_p$) corresponds to a local unshifted, $V_0 = 0$, Maxwellian distribution with a uniform ion temperature, $T_0 = 400$ eV, and the background density profile, n_0, shown in Figure 4a. Small-level perturbations, $\delta n \sim 1.0 \times 10^{-4} \cos(96\theta - 32\phi)$, are introduced in the initial density distribution.

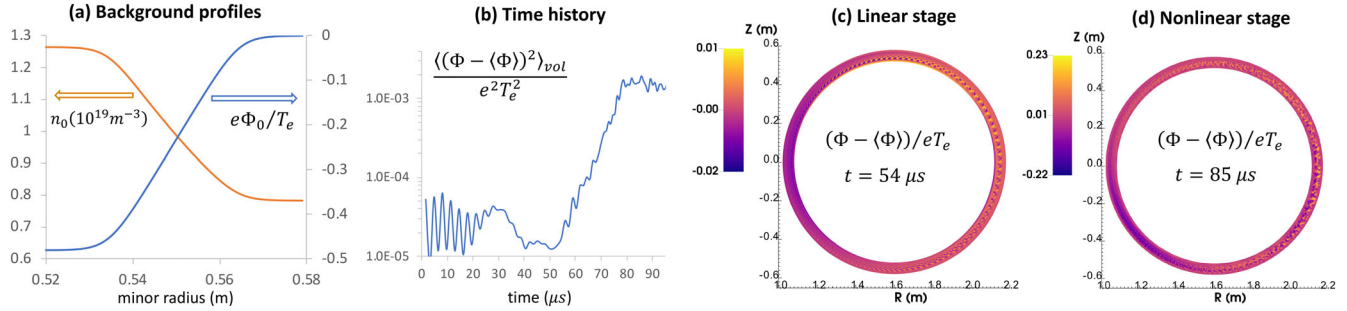

FIGURE 4 COGENT simulations of the resistive-drift ballooning turbulence with the electromagnetic hybrid model. Frame (a) shows the initial profiles for the ion density and the electrostatic potential. Frame (b) shows the time history for the mapped-space volume average of the squared non-zonal component of electrostatic potential variations, $\left\langle(\Phi/eT_e-\langle\Phi/eT_e\rangle)^2\right\rangle_{vol}$. Here, $\langle\chi\rangle_{vol}=N^{-1}\sum\chi_{i,j,k}$ corresponds to a sum over the spatial indices (i,j,k) divided by the total number of spatial cells, N. Frames (c) and (d) show the non-zonal component of electrostatic potential variations corresponding to the linear and nonlinear stages, respectively.

The electron temperature is taken as uniform with $T_e = 400$ eV and an artificially increased uniform value of the electron collisionality corresponding to $\tau_e V_{T_e}/(qR_0) = 0.5$ is adopted for the plasma conductivity. To minimize initial transient perturbations, the electrostatic potential is initialized with the Boltzmann equilibrium profile, $\Phi_0 = -(T_0/e)\ln(n_0/C)$, where the constant C is determined from a zero Dirichlet boundary condition at the outer radial boundary. The parallel vector potential is initialized as $A_{\|,0} = 0$. Finally, we subtract the initial value of the RHS in Equation (5) from itself to force $\Phi = \Phi_0(r)$ and $A_\| = 0$ as an equilibrium solution to Equation (5) and Equation (8) in the absence of perturbations and the polarization density correction.

Results of the illustrative COGENT simulations including the linear and nonlinear stages are shown in Figure 4. A periodic toroidal wedge with $\Delta\phi = 2\pi/8$ is considered and a single toroidal block is used. The grid resolution is specified by $(N_r, N_\phi, N_\theta, N_{v\|}, N_\mu) = (64, 4, 2048, 32, 24)$, and the velocity space extent is given by $-4.9\sqrt{T_0/m_i} \le v_\| \le 4.9\sqrt{T_0/m_i}$ and $0 \le \mu \le 10.9T_0R_0/|I|$. The stable time step is set by the Courant constraint for the ion advection in the radial direction. During the initial stage, when the radial advection velocity is dominated by the magnetic drifts, the time step corresponds to $\Delta t \approx 0.16$ μs. In the nonlinear stage, the radial advection velocity is apparently dominated by the $E \times B$ velocity, and the stable time step drops to $\Delta t \approx 0.08$ μs. The simulations are performed on 1024 CPU cores of the NERSC Perlmutter cluster, and it takes about 25 s of wall clock time per step for the IMEX time integration. About 10 iterations are required to reduce the GMRES solver residual by six orders of magnitude. Recall that the preconditioner operator neglects the polarization density corrections [the last term on the RHS of Equation (11)] in addition to other approximations as discussed in detail in Section 2.2. The IMEX approach requires only about 20% more wall clock time per step as compared with the fully explicit (RK4) approach, for which a stable time step is found to be about six times smaller during the linear stage. Note that for more realistic plasma parameters involving stronger density variations between the core and the edge region, the explicit time step limitations arising from the fast Alfvén wave propagation in a low-density region would be substantially more severe. Also, the IMEX time step limitation imposed by the ion advection can be relaxed by making use of our recently developed implicit scheme that can handle an advection operator.[10] This can further improve the performance of COGENT hybrid electromagnetic simulations.

5 | CONCLUSIONS

An electromagnetic gyrokinetic ion-fluid electron hybrid model is developed and implemented in the COGENT code. The model involves the long-wavelength limit of the 5D full-F ion gyrokinetic equation coupled to the 3D vorticity and Ohm's law equations for the electrostatic and electromagnetic potentials and to an isothermal fluid response for the electron species. To step over the fast shear Alfvén wave time scale, an implicit-explicit (IMEX) time integration combined with the physics-based preconditioning is used. The preconditioner (PC) captures linear Alfvén wave dynamics and includes the effects of the plasma resistivity and electron inertia. The PC implementation requires solving a set of 3D elliptic equations, which is facilitated by making use of multigrid methods. Since the fast time scales are confined within the low-dimensional 3D fluid/field part of the hybrid system, only a modest computational overhead is anticipated from using the IMEX approach.

The fluid/field part of the hybrid system is verified in 3D slab fluid simulations of the drift-resistive instability, performed for both Cartesian and field-aligned grid systems. The performance of the IMEX approach, coupled with physics-based preconditioning, is then investigated in 3D toroidal fluid simulations of the resistive ballooning mode. A stiff case with an implicit-to-explicit time step ratio of 50 is considered, demonstrating an 11x runtime speed- up. Finally, the 5D/3D hybrid model is applied to toroidal simulations of resistive-drift ballooning turbulence. Only a modest increase in computational cost per time step is observed between the IMEX and a fully explicit method (RK4), whereas the IMEX approach enables a significantly larger stable time step.

ACKNOWLEDGMENTS

The authors are grateful to M. Umansky for fruitful discussions. This research was supported by the U.S. Department of Energy under contract DE-AC52-07NA27344.

DATA AVAILABILITY STATEMENT

The data that support the findings of this study are available from the corresponding author upon reasonable request.

REFERENCES

[1] S. K. R. Hager, S. Ku, A. Y. Sharma, C. S. Chang, R. M. Churchill, A. Scheinberg, *Phys. Plasmas* **2022**, *29*, 112308.
[2] D. Michels, P. Ulbl, W. Zholobenko, T. Body, A. Stegmeir, T. Eich, M. Griener, G. D. Conway, F. Jenko, *Phys. Plasmas* **2022**, *29*, 032307.
[3] N. R. Mandell, A. Hakim, G. W. Hammett, M. Francisquez, *J. Plasma Phys.* **2020**, *86*, 905860109.
[4] B. D. Scott, *Plasma Phys. Controlled Fusion* **2007**, *49*, S25.
[5] B. Dudson, J. Leddy, *Plasma Phys. Controlled Fusion* **2017**, *59*, 054010.
[6] X. Q. Xu, B. D. Dudson, P. B. Snyder, M. V. Umansky, H. R. Wilson, T. Casper, *Nucl. Fusion* **2011**, *51*, 103040.
[7] B. I. Cohen, M. V. Umansky, W. M. Nevins, M. A. Makowski, J. A. Boedo, D. L. Rudakov, G. R. McKee, Z. Yan, R. J. Groebner, *Phys. Plasmas* **2013**, *20*, 055906.
[8] W. Zholobenko, T. Body, P. Manz, A. Stegmeir, B. Zhu, M. Griener, G. D. Conway, D. Coster, F. Jenko, *ASDEX Upgrade Team* **2021**, *63*, 034001.
[9] M. Dorf, M. Dorr, *Phys. Plasmas* **2021**, *28*, 032508.
[10] M. Dorf, M. Dorr, D. Ghosh, M. Umansky, IAEA conference. **2023**.
[11] M. Dorf, M. Dorr, *Contrib. Plasma Phys.* **2018**, *58*, 434.
[12] M. A. Dorf, M. R. Dorr, J. A. Hittinger, R. H. Cohen, T. D. Rognlien, *Phys. Plasmas* **2016**, *23*, 056102.
[13] M. Dorf, M. Dorr, *Contrib. Plasma Phys.* **2022**, *62*, e202100162.
[14] C. A. Kennedy, M. H. Carpenter, *Appl. Numer. Math.* **2003**, *44*, 139.
[15] D. Ghosh, M. A. Dorf, M. R. Dorr, J. A. F. Hittinger, *J. Sci. Comput.* **2018**, *77*, 819.
[16] D. A. Knoll, D. E. Keyes, *J. Comput. Phys.* **2004**, *193*, 357.
[17] *hypre: High Performance Preconditioners*. https://github.com/hypre-space/hypre/wiki/Citing-HYPRE
[18] S. I. Braginskii, *Rev. Plasma Phys.* **1965**, *1*, 205.
[19] Y. Saad, Iterative Methods for Sparse Linear Systems, 2nd ed., Society for Industrial and Applied Mathematics, Philadelphia, USA **2003, 184**.
[20] B. Dudson, S. Farley, Lois Curfman McInnes. arXiv **2012** (1209.2054).
[21] F. Hariri, M. Ottaviani, *Comput. Phys. Commun.* **2013**, *184*, 2419.
[22] F. X. Giraldo, J. F. Kelly, E. M. Constantinescu, *SIAM J. Sci. Comput.* **2013**, *35*, B1162.

How to cite this article: M. Dorf, M. Dorr, D. Ghosh, *Contrib. Plasma Phys.* **2024**, e202300114. https://doi.org/10.1002/ctpp.202300114